Distortion-free magnetic resonance imaging in the zero-field limit

Nathan Kelso [a,c], Seung-Kyun Lee [a,c,1], Louis-S. Bouchard [b,c,2], Vasiliki Demas [b,c,3], Michael Mück [d], Alexander Pines [b,c], John Clarke [a,c,*]

[a] Department of Physics, University of California, Berkeley, CA 94720, USA
[b] Department of Chemistry, University of California, Berkeley, CA 94720, USA
[c] Materials Sciences Division, Lawrence Berkeley National Laboratory, Berkeley, CA 94720, USA
[d] Institut für Angewandte Physik, Justus-Liebig-Universität Gießen, D-35392 Gießen, Germany

ARTICLE INFO

ABSTRACT

MRI is a powerful technique for clinical diagnosis and materials characterization. Images are acquired in a homogeneous static magnetic field much higher than the fields generated across the field of view by the spatially encoding field gradients. Without such a high field, the concomitant components of the field gradient dictated by Maxwell's equations lead to severe distortions that make imaging impossible with conventional MRI encoding. In this paper, we present a distortion-free image of a phantom acquired with a fundamentally different methodology in which the applied static field approaches zero. Our technique involves encoding with pulses of uniform and gradient field, and acquiring the magnetic field signals with a SQUID. The method can be extended to weak ambient fields, potentially enabling imaging in the Earth's field without cancellation coils or shielding. Other potential applications include quantum information processing and fundamental studies of long-range ferromagnetic interactions.

© 2009 Elsevier Inc. All rights reserved.

1. Introduction

In MRI, the Larmor precession frequency $\omega(x, y, z) = \gamma B(x, y, z)$ of the proton spins in the position-dependent magnetic field $B(x, y, z)$ frequency- and phase-encodes the proton density distribution into a magnetic signal that is subsequently decoded to form an image [1] (γ is the magnetogyric ratio). In clinical MRI machines [1] the strength of the applied homogeneous static magnetic field $\boldsymbol{B_0} = B_0 \hat{z}$ is typically 1.5 T. There has been recent interest, however, in systems operating in magnetic fields of the order of 10^{-4} T (for example [2–7]), where T_1-weighted contrast is significantly enhanced [5] (T_1 is the longitudinal relaxation time). The loss of polarization is compensated—at least in part—by prepolarizing [8] the spins at a much higher field, or by hyperpolarization techniques using lasers [9], dynamic nuclear polarization [10,11] or parahydrogen-induced polarization [12]. As the frequency is lowered, the loss of signal amplitude inherent in Faraday-Law detection is mitigated by detecting the nuclear magnetization with either a Superconducting QUantum Interference Device (SQUID) [13] or an atomic magnetometer [14], both of which respond to the magnetic flux itself, rather than its time rate of change. Regardless of the magnitude of B_0, all currently used imaging processes involve the superposition of magnetic field gradients on a static field to impose spatial variations of the total field across the subject or sample. In the zero static field regime reported here, conventional MRI gradients are unable to encode the spins along a given direction and Fourier encoding breaks down.

2. Theory

In conventional MRI techniques, the applied magnetic field gradients are assumed to be linear and unidirectional so that the field due to gradients is given by $\boldsymbol{B}(x, y, z) = (G_x x + G_y y + G_z z) \hat{z}$, where $G_x = \partial B_z/\partial x$, $G_y = \partial B_z/\partial y$, and $G_z = \partial B_z/\partial z$ are constants [1]. As an example, $\boldsymbol{B}(x, y, z) = G_z z \hat{z}$ is shown in Fig. 1a. In reality, however, such idealized gradients are forbidden by the Maxwell equations $\mathrm{div}\boldsymbol{B} = \mathrm{curl}\boldsymbol{B} = 0$ for any time-independent magnetic field $\boldsymbol{B}$ in free space. In fact, any gradient must be accompanied by concomitant gradients in at least one additional direction, as illustrated in Fig. 1b. At very low static fields the undesired gradient components perpendicular to $\boldsymbol{B_0}$ induce severe image distortions [15–17]. The degree of distortion is characterized by a parameter $\varepsilon = GL/B_0$, where G is the magnitude of the field gradient and L is the image field of view (FOV) [17]. When $\varepsilon \ll 1$, the gradient fields can be approximated as unidirectional, greatly simplifying image encoding and reconstruction and leading to negligible image distortion.
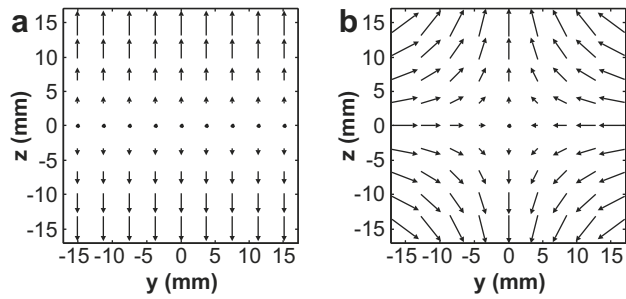
Fig. 1. Idealized and achievable magnetic field gradients. (a) Idealized gradient field $\boldsymbol{B} = (\partial B_z/\partial z)z \ \hat{z}$. Such a field violates Maxwell's equations. (b) Example of a realizable gradient field in the y–z plane of the form $\boldsymbol{B}(y, z) = (\partial B_y/\partial y)y \ \hat{y} + (\partial B_z/\partial z)z \ \hat{z}$. Lengths of vectors represent relative field strengths.

This "truncation" of the concomitant fields forms the basis of nearly all MRI techniques used today including projection reconstruction and Fourier imaging [1].

Several approaches have been proposed for imaging in the regime $\varepsilon \gg 1$ where conventional techniques fail [18–20]. Our experiment relies on the fact that, for very small angles, the precession of spins about an arbitrary field $\boldsymbol{B}$ can be represented by the sum of the precessions about each component of $\boldsymbol{B}$ [18]. After such a precession, the magnetization components that have evolved in the concomitant field can be reversed while leaving the desired unidirectional encoded component unchanged, an example of an average Hamiltonian [21]. Fig. 2a shows the pulse sequence for two-dimensional imaging in the limit of zero static field, and Fig. 2b and c depicts the classical evolution of spins at (y', z') subjected to this sequence. The proton spins are first polarized along the x-axis by a large field B_p which is turned off nonadiabatically [11] at time $t = 0$ (point A in Fig. 2a–c). The gradient field with the approximate form (cross terms have been neglected)

$$\boldsymbol{B}(y,z) = (\partial B_y/\partial y)y \ \hat{y} + (\partial B_z/\partial z)z \ \hat{z} \tag{1}$$

is turned on, and subsequently turned off nonadiabatically at time τ (point B). During this time interval, the spin precesses about $\boldsymbol{B}(y', z')$. The time τ is chosen to satisfy the requirement $\tau \ll 1/\gamma G_z L$. Consequently, the precession during the interval τ is small, and we can treat it as the sum of precessions around $\hat{z}$ and $\hat{y}$: $\delta_z = \gamma(\partial B_z/\partial z)z'\tau$ around $\hat{z}$ (Fig. 2b) and $\delta_y = \gamma(\partial B_y/\partial y)y'\tau$ around $\hat{y}$ (Fig. 2c). After the gradient pulse, a π pulse of uniform field B_π is applied along the z-axis with amplitude and duration adjusted to produce a precession angle of π around $\hat{z}$. This pulse flips the spin to the point C in Fig. 2b and c. Subsequently, a second gradient pulse brings the spin to D, and a second π pulse to E. This sequence of pulses produces a net precession of the spin about B_z, but no net precession about B_y. Thus, the two π pulses average out the components of field perpendicular to $\hat{z}$, leaving an effectively unidirectional gradient field $\boldsymbol{B}_{\mathrm{eff}}(y, z) = G_z z \ \hat{z}$.

To implement this sequence, it is convenient to define a "pulse unit" consisting of two gradient pulses and two π pulses. Clearly, the addition of subsequent pulse units increases the angle of precession about $\hat{z}$. After n pulse units, the gradient has been applied for a total time $t_n = 2n\tau$. Data are acquired at discrete values of k, namely

$$k(t_n) = \gamma \int_0^{t_n} G_z(t)dt, \tag{2}$$

using point-by-point detection in which each point in k-space is acquired in a separate experiment. After the final pulse unit, a small measurement field B_m is turned on along the z-axis and the NMR signal from precession about this field is detected (Fig. 2d). The Fourier transform of this real-valued signal produces a complex-valued
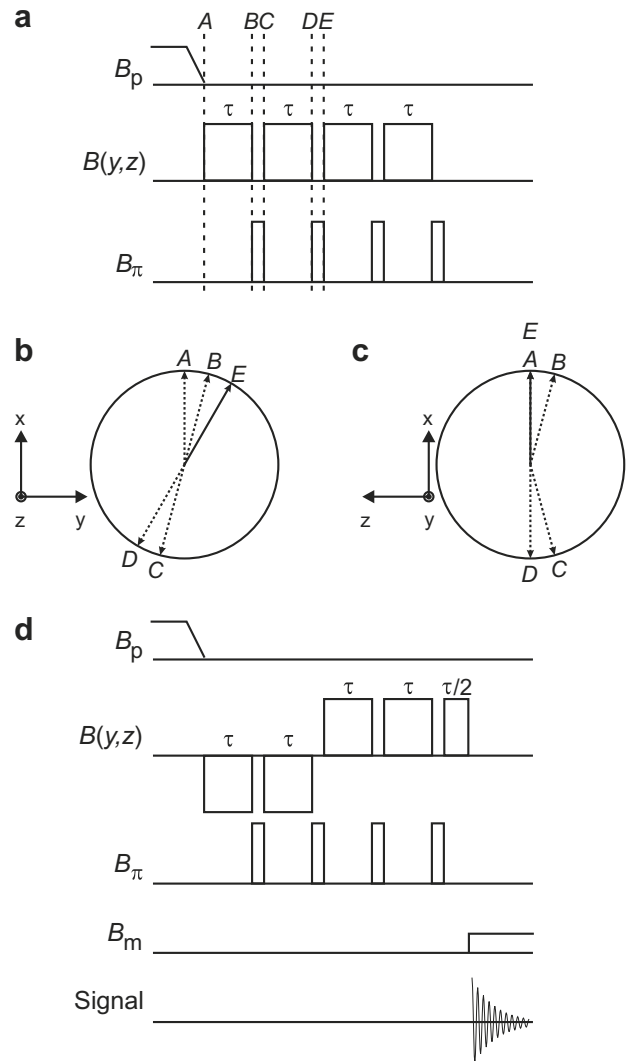
Fig. 2. Protocol for MRI in zero static field. (a) Pulse sequence vs. time. (b and c) Progression of the spin vector at times $t = 0$ (A), τ (B), 2τ (C), 3τ (D) and 4τ (E) about (b) z-axis and (c) y-axis. (d) Pulse sequence used for the zero-field MRI experiment differs from that in b in two respects. First, after the final pulse pair, a gradient pulse was applied for a time $\tau/2$; this pulse corrects higher order errors [18,19]. Second, to ensure that the important $k = 0$ point was included, the gradient was inverted in the first pulse unit, so that the first point in k-space was $k(5\tau/2) = -(3\tau/2)\gamma G_z$. All subsequent gradient pulses have positive polarity; for example, the second k-space point was $k(9\tau/2) = (\tau/2)\gamma G_z$. Note that the measurement field B_m is *not* applied during encoding pulses; it is used solely for point-by-point k-space acquisition, enabling quadrature detection with a single sensor.

peak in frequency space, yielding the real and imaginary parts of the signal at $k(2n\tau)$. After completing the acquisition, the k-space projection is Fourier transformed to obtain a one-dimensional, real-space projection of the sample. Subsequently, we rotate the sample through an angle θ ($\ll\pi$) and acquire another projection; the procedure is repeated until the range from $0°$ to $180°$ is covered. The image is reconstructed using filtered back-projection [1].

3. Experimental methods

The experimental configuration is shown schematically in Fig. 3. A double-walled Pyrex vacuum vessel is immersed in liquid helium contained in a dewar surrounded with a single-layer mu-metal shield to attenuate external magnetic fields. A superconducting lead shield inside the dewar stabilizes the residual magnetic
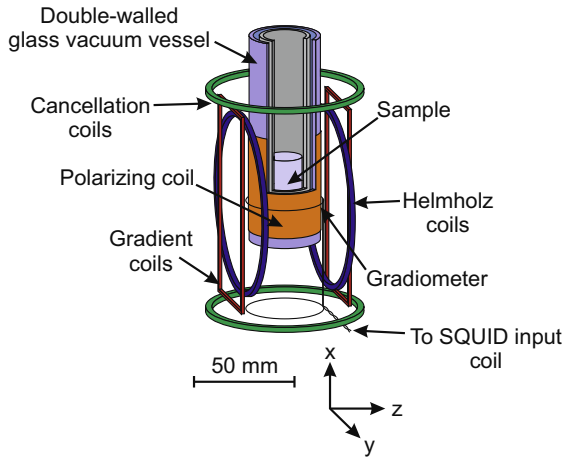
Fig. 3. Configuration of experiment.

field. The sample rests at the bottom of the insert—which has room-temperature access—and is maintained in the liquid state at approximately $-50\,°C$ by a heater; the heater is switched off during encoding and data acquisition [22]. The coils required to generate the magnetic fields are wound from insulated NbTi wire and are attached to the outside of the insert. A Helmholtz pair provides a uniform field along the z-axis for the π pulses, and a second Helmholtz pair, wound on top of the first, generates the measurement field B_m. The rectangular gradient coils generate a field with the approximate form

$$\boldsymbol{B}(y,z) = (\partial B_y/\partial y)y\hat{y} + (\partial B_z/\partial z)z\hat{z} \qquad (3)$$

in the y–z plane (shown in Fig. 1b) over the imaging FOV, where $\partial B_y/\partial y \approx -0.9\,(\partial B_z/\partial z)$; we neglect the cross terms and terms higher than first order in the gradient. Since we image in the y–z plane, we also neglect the effects of gradients along $\hat{x}$. A further pair of coils largely cancels the residual field from the Earth, which is predominantly along the x-axis. The signal from the precessing spins is detected by a first-derivative, superconducting gradiometer coupled to the input coil of a Nb-based SQUID [13]. The gradiometer, which consists of two Nb-wire loops of nominally equal area wound

in opposite senses and connected in series, reduces ambient noise in the measurement direction. A series array of 24 Josephson junctions limits the supercurrent while the fields are being switched [23]. The SQUID is enclosed in a Nb shield suspended below the insert, and is read out using a flux-locked loop [13].

4. Results

Our results are shown in Fig. 4. Fig. 4a shows the geometry of the phantom in an image acquired in a 9.4-T MRI system with a FOV of 23 mm. Fig. 4b shows the image obtained with a gradient echo sequence in an applied static field of 0.12 μT, corresponding to an NMR frequency of ~5 Hz, applied along the z-axis. The image was acquired using point-by-point detection (see Appendix A). We have independently measured the residual field B_r arising from imperfect shielding, and estimate that the sum of the applied and residual fields yields $\varepsilon > 6.5$. As expected, in this regime of strong concomitant gradients, Fourier encoding breaks down and the image bears no resemblance to the phantom [15–17].

Fig. 4c shows the image acquired in zero applied field with the sequence shown in Fig. 2d. We minimized the residual field B_r by performing separate NMR experiments while varying the cancellation field along the x-axis. The minimum NMR frequency was about 8 Hz, corresponding to $B_r \approx 0.2\,\mu T$. With a FOV $L = 23$ mm, gradient pulse magnitude $G_z = 100\,\mu T/m$, and regarding the residual field as B_0, we find $\varepsilon > 10$, a regime which is clearly beyond the realm of conventional MRI. Our image, however, closely resembles the high-field image. Acquisition of this image required 5.6 h; in Appendix B we illustrate how this time could potentially be reduced to a few minutes.

5. Discussion

We can generalize our zero-field technique to the case of a uniform ambient field B_a, which imposes conditions on both the gradient and π pulses. For a given amplitude, the maximum gradient pulse duration is limited by the need to keep the precession angle small. In practice, though, we find that the zero-field sequence is quite robust—in the image shown in Fig. 4c, the maximum precession angle is approximately 65°. For a total field of 50 μT (approximately the Earth's field), an upper bound of 65° limits
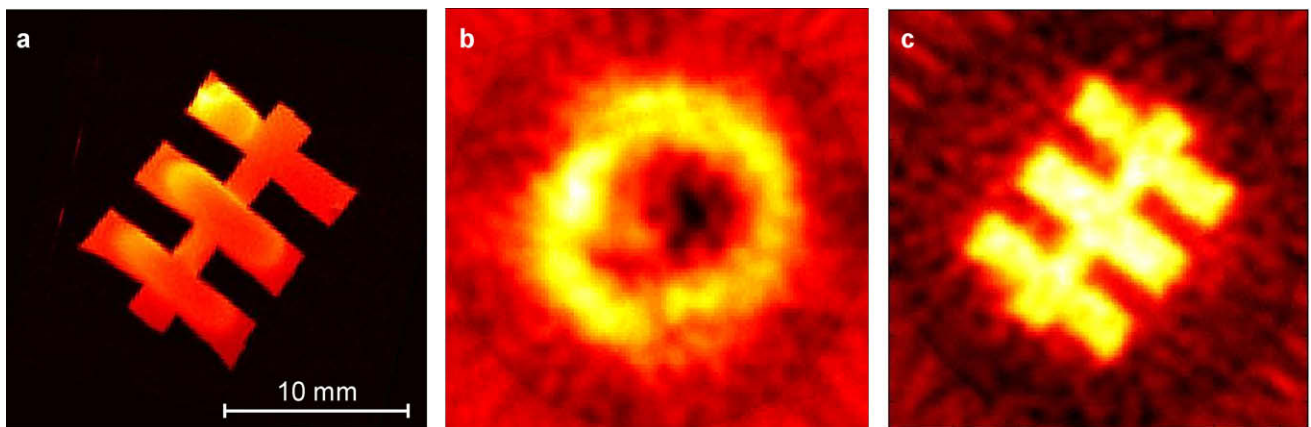

Fig. 4. Images of a phantom. Views are along the axis of a nylon cylinder 17 mm in diameter and 35 mm long in which a cavity has been cut and filled with water (a) or ethanol (b and c). (a) High-field conventional image acquired at 9.4 T. (b) Conventional gradient-echo image with $\varepsilon > 6.5$ bears no relation to the phantom due to concomitant field distortions. (c) Image encoded in the approach to zero applied static field where the concomitant fields of the encoding gradients yield $\varepsilon > 10$. The prepolarization field $B_p \approx 10$ mT was applied for 2 s. The image was encoded in nearly zero static field using 100-μT/m gradient pulses with a duration $\tau = 5$ ms. The π pulses, with a magnitude of approximately 12 μT and duration of 1 ms, produced an effective field $\boldsymbol{B}_{eff} = (\partial B_z/\partial z)z\,\hat{z}$. The π pulse amplitude was determined in separate experiments to an accuracy of ±1%. After the spins were encoded, the NMR signal was acquired in 1 s in a measurement field $B_m = 3.75$ μT, corresponding to an NMR frequency of 160 Hz. Projections were acquired every 7.5°, so that 24 projections covered the range from 0° to 172.5°. The time for each projection was about 14 min, giving a total acquisition time of about 5.6 h. Each k-space projection contained 24 points.

the maximum duration of the gradient pulse to about 85 µs: the angle of precession during a field pulse of amplitude B and duration τ is given (in radians) by $\delta = \gamma B \tau$. For $\delta = 65° \approx 1.13$ radians, $\gamma = 2\pi \times 42.6$ Hz/µT, and $B = 50$ µT we find $\tau \approx 85$ µs. The presence of B_a also affects the amplitude and duration of the π pulse. Components of B_a perpendicular to the π pulse induce errors by modifying the pulse amplitude and direction. To limit the error in the π pulse to less than 1%, the pulse amplitude must be approximately seven times the perpendicular component of B_a. This requirement can be mitigated, however, by aligning the π pulse with B_a. Components of B_a parallel to the direction of the π pulse, B_a (*parallel*), can be beneficial; the total field during the π pulse is

$$B_\pi = B_\pi(app) + B_a(parallel), \qquad (4)$$

where $B_\pi(app)$ is the applied π pulse. Thus, if one aligns the system so that B_π is parallel to (say) the Earth's field to within about 8°, one can keep errors in the π pulse amplitude to less than 1% and acquire undistorted images (see Appendix C).

A general comment about concomitant gradient problems is in order. While distortion errors arising from small values of ε can be corrected for by post-processing or pulse sequence design [16], the general problem of arbitrary ε is considered intractable [17]. This does not mean that reconstruction algorithms for general B-field distributions cannot be devised, but that the general reconstruction mapping problem becomes more ambiguous and ill-defined. For example, information would be entirely lost for all spatial locations at which the local magnetic field points parallel to the axis of a Faraday detector loop. If the exact field distribution is known and enough detectors are used, it should be possible to detect and reconstruct all image information using, for example, an array of carefully positioned detectors and inverting by taking appropriate linear combinations (see Bouchard and Anwar [24] for a formalism which could be adapted). Hennig and co-workers [25] have shown that nonlinear gradients that vary in direction do not pose problems; however their image reconstruction method assumes a uniform axis of quantization, which is not the case here. The method proposed in this article has the important advantage that it does not require an array of detectors. Finally, we have used SQUID detection for this demonstration because it works well in the zero-field limit, but our method could be used with any suitable detector, such as an optical atomic magnetometer [26]. In fact, the latter option would seem to be more convenient for a portable MRI device.

6. Conclusions

In conclusion, we have demonstrated experimentally how to eliminate the effects of concomitant gradients so that MRI in a pure gradient field can be performed. With further improvements in the pulse sequence and hardware, as discussed in Appendices B and C, and recent developments in non-cryogenic detection (e.g. [26]), the prospect of low-field, portable MRI in a residual field is encouraging. The extension to larger FOV is also possible, but would place more demands on the hardware. In theory, there is no limit to the FOV as long as the π pulses are short enough to permit the acquisition of enough data points during a T_2-limited period. If we ignore detector dead times, in practice this becomes an issue of maximum peak power which still presents substantial advantages over a continuously applied uniform truncating field. Producing the latter consumes more power and requires a careful arrangement of coils to make the field homogeneous over a large volume, whereas our method would take advantage of the naturally homogeneous Earth's magnetic field. From this point of view, we believe our approach to be a competitive candidate for portable MRI applications.

We note that our experimental demonstration utilizes a sample with cylindrical symmetry. This was done out of convenience and simplicity. The extension to 3D MRI is completely straightforward provided additional gradient and π-pulse coils are added to the setup. Multislice MRI should also be possible with the use of slice selection, in a manner similar to that described in [20].

In addition to MRI, we envisage applications of our pulsed technique or related continuous-wave versions [20] to experiments that use magnetic field gradients for controlling the dynamics of spins. For example, several proposals for quantum information processing [27–29] use magnetic fields and field gradients to confine ions or electrons in one-[27] or two-dimensional [29] arrays of traps. The analysis presented by Ciaramicoli et al. [29] clearly shows that the presence of concomitant gradients makes it nontrivial to address individual qubits in higher dimensional arrays. Our technique could be used [30] to provide unidirectional and linear gradients in the field to address individual spins or groups of spins in three-dimensional space in a relatively straightforward manner. This addressing scheme would also enable the creation of controlled quantum Ising spin models for fundamental studies of long-range ferromagnetic interactions [29] in arbitrary, user-designed lattices.

Appendix A. Gradient echo imaging

The image shown in Fig. 4c was acquired using a conventional gradient echo sequence [1] modified for point-by-point k-space acquisition. The sequence used to acquire the $k(9\tau/2)$ point is shown in Fig. 5. The proton spins are first polarized along the x-axis by a large field B_p which is turned off nonadiabatically at time $t = 0$. Subsequently, two fields are switched on: a uniform static field B_0 along the z-axis, and a negative gradient field

$$-\boldsymbol{B}(y,z) = -(\partial B_y/\partial y)y\,\hat{y} - (\partial B_z/\partial z)z\,\hat{z}. \qquad (A.1)$$

After a time 2τ the gradient is reversed. The B_0 and gradient fields are maintained until the desired point in k-space is reached, at which time a measurement field B_m is applied. The time-domain data are acquired and processed as described in the main text for the zero-field experiment.
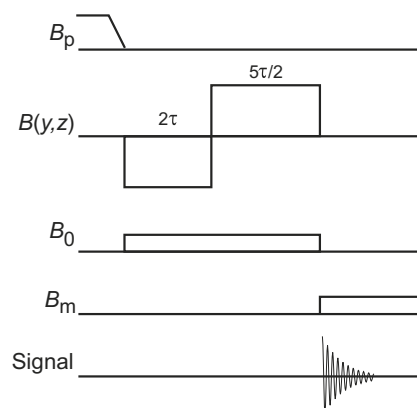

Fig. 5. Pulse sequence vs. time for the $k(9\tau/2)$ point of the conventional image.

The point-by-point k-space acquisition technique was used in the conventional image in order to match as closely as possible the conditions for the zero-field image. The conventional imaging experiment uses the same polarizing pulse, gradients, and encoding times as does the zero-field experiment. The gradient echo sequence requires a uniform static field B_0 during encoding in order to establish a "preferred" gradient direction; components of the gradient perpendicular to B_0 are the unwanted concomitant terms (recall that in the zero-field sequence, the preferred gradient direction is that of the π pulses).

Appendix B. Imaging time considerations

Our implementation of zero-field MRI involves acquiring k-space point-by-point. The primary reason is that this method yields the real and imaginary parts of k-space, effectively providing quadrature detection with a single sensor, but the procedure is time consuming. For each of the 24 projections of the image we acquire 24 points, each taking 3.5 s (2-s polarizing pulse followed by up to 0.5-s encoding time and 1-s data acquisition time), and each point is averaged 10 times to increase the signal-to-noise ratio (SNR) leading to a total acquisition time of about 5.6 h. The imaging time could be reduced substantially by using two orthogonal SQUID-based gradiometers. Since all points in one projection could be acquired in one experiment, the imaging time would be reduced by a factor of 24. Increasing the prepolarization field from 10 mT to 100 mT would increase the SNR 10-fold. As shown below, these two factors alone would reduce the acquisition time to 2–3 min. Adding a Helmholtz pair along the y-axis (to allow π pulses in an arbitrary direction in the y–z plane) and a second, off-diagonal gradient such as $\partial B_z/\partial y$ would make it possible to perform acquisitions along arbitrary k-space trajectories, and would eliminate the need to rotate the sample. Optimized k-space sampling would result in further improvements in image quality and acquisition time.

We now outline our calculations of the statements above. In MRI, the SNR is commonly defined as the signal amplitude divided by the standard deviation of the noise. For an acquisition time t_{acq}

$$SNR = \frac{\int_0^{t_{acq}} s(t)dt}{\sqrt{\int_0^{t_{acq}} \sigma_n^2 dt}} = \left[\frac{\int_0^{t_{acq}} s(t)dt}{\sqrt{t_{acq}}}\right]\frac{1}{\sigma_n}, \tag{B.1}$$

where σ_n is the standard deviation of the noise and $s(t)$ is the integrated signal from the nuclear magnetization detected by the sensor (assuming negligible noise) [1]. To compare the SNR of two acquisition methods, we estimate the value of the bracketed term from the formula

$$s(t) \propto \int_y \int_z m(y,z) \exp\left[-t/T_2^*\right] \exp\left[-i\gamma t B_G(y,z)\right] dydz, \tag{B.2}$$

where T_2^* is the transverse relaxation time, $B_G(y, z)$ is the field due to applied gradients, and $m(y, z)$ is a function representing the spin distribution in the sample, normalized such that

$$\int_y \int_z m(y,z)dydz = 1. \tag{B.3}$$

The standard deviation of noise is time-independent and assumed to originate from the sample, detector, and electronics, which are the same in both acquisition methods; therefore, the σ_n term has been omitted from the following comparison.

In the point-by-point (pbp) acquisition method described in the text, the signal is acquired as a free induction decay (FID) in the uniform field B_m. The demodulated signal equation in this case is given by

$$s_{pbp}(t) = \int_y \int_z m(y,z) \exp\left[-t/T_2^*\right] dydz, \tag{B.4}$$

where, in our experiments, the transverse relaxation time T_2^* was measured to be 300 ms. Using our acquisition time t_{acq} = 1 s,

$$SNR_{pbp} \propto \frac{\int_0^{t_{acq}} s_{pbp}(t)dt}{\sqrt{t_{acq}}} \approx 0.289. \tag{B.5}$$

In a directly-detected experiment using two orthogonal detectors, the signal could be detected as precession about the gradient field $\boldsymbol{B_G}$ during every second gradient pulse. The demodulated signal equation in this case is given by

$$s_{dir}(t) = \int_y \int_z m(y,z) \exp\left[-t/T_2^*\right] \exp\left[-i\gamma t B_G\right] dydz, \tag{B.6}$$

where

$$B_G = \sqrt{\left[(\partial B_y/\partial y)y\right]^2 + \left[(\partial B_z/\partial z)z\right]^2} \tag{B.7}$$

is the field magnitude at the point (y, z). For our value B_G = 100 µT/m and a 5-ms acquisition, we find

$$SNR_{dir} \propto \frac{\sqrt{2}\int_0^{t_{acq}} s_{dir}(t)dt}{\sqrt{t_{acq}}} \approx 0.0990. \tag{B.8}$$

The factor of $\sqrt{2}$ arises from the use of two detectors in quadrature detection.

We now compare the difference in SNR between the two acquisition methods. If the noise standard deviation σ_n is the same in both cases, we find

$$\frac{SNR_{dir}}{SNR_{pbp}} \propto \frac{0.0990}{0.289} \approx 0.34. \tag{B.9}$$

The SNR in the directly-detected experiment is about 1/3 that of the point-by-point experiment, while the imaging time is reduced by a factor of 24.

As stated in the main text, our point-by-point imaging procedure took approximately 5.6 h; the time is long because each k-space point is acquired in a separate experiment. The imaging time could potentially be reduced to approximately two minutes, for the equivalent SNR, by acquiring the signal directly (using two orthogonal detectors), eliminating signal averaging, and increasing the polarizing field from 10 mT to 100 mT.

We explain this estimate as follows. The direct acquisition method would reduce imaging time by a factor of 24 by acquiring all k-space points in a single experiment. The SNR loss, however, is a factor of $\sim$3, as described previously. Elimination of signal averaging reduces imaging time by an additional factor of 10, at the cost of an additional factor of $\sim$3 in SNR. Thus, the total SNR drops by a factor of $\sim$9 while reducing imaging time by a factor of 240. This factor of $\sim$9 loss in SNR can be recovered by increasing the prepolarization field from 10 to 100 mT. Together, these factors result in the same SNR, but with a substantial reduction in acquisition time.

Appendix C. Effect of a uniform ambient field on π pulse amplitude

We consider the conditions on the π pulse imposed by the presence of a uniform ambient field. The z-axis is defined to be along the direction of the applied π pulse. The z-axis is thus the desired direction of the total π pulse. In the presence of an ambient field the field amplitude along z is given by B_π (*app*) + B_a (*parallel*), where B_π (*app*) is the applied pulse and B_a (*parallel*) is the component of ambient field parallel to the z-axis. For a component of
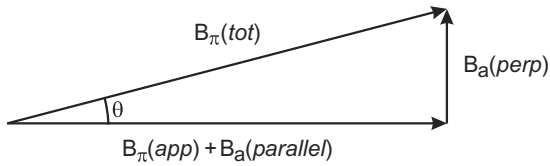
Fig. 6. Effect of uniform ambient field on π pulse.

ambient field perpendicular to the z-axis B_a (perp), the total field during the π pulse is given by (Fig. 6)

$$B_\pi(tot) = \sqrt{[B_\pi(app) + B_a(parallel)]^2 + [B_a(perp)]^2}. \tag{C.1}$$

Thus

$$B_\pi(tot) \leqslant 1.01[B_\pi(app) + B_a(parallel)] \tag{C.2}$$

for B_a (perp) $\leqslant B_\pi$ (tot)/7.

For the limiting case in which B_π (app) = 0, the angle θ in Fig. 6 gives the misalignment between B_a and the z-axis. To maintain the condition B_a (perp) $\leqslant B_\pi$ (tot)/7, one requires $\theta \leqslant 8°$.

References

[1] E.M. Haacke, R.W. Brown, M.R. Thompson, R. Venkatesan, Magnetic Resonance Imaging: Physical Principles and Sequence Design, Wiley, New York, 1999; P.T. Callaghan, Principles of Nuclear Magnetic Resonance Microscopy, Oxford University Press, Oxford, 1994.

[2] P.T. Callaghan, M. Le Gros, Nuclear spins in the Earth's magnetic field, Am. J. Phys. 50 (1982) 709–713.

[3] J. Stepišnik, V. Eržen, M. Kos, NMR imaging in the earth's magnetic field, Magn. Reson. Med. 15 (1990) 386–391.

[4] S. Xu, V.V. Yashchuk, M.H. Donaldson, S.M. Rochester, D. Budker, A. Pines, Magnetic resonance imaging with an optical atomic magnetometer, Proc. Natl. Acad. Sci. USA 103 (2006) 12668–12671.

[5] J. Clarke, M. Hatridge, M. Mößle, SQUID-detected magnetic resonance imaging in microtesla fields, Annu. Rev. Biomed. Eng. 9 (2007) 389–413.

[6] V.S. Zotev, A.N. Matlashov, P.L. Volegov, I.M. Savukov, M.A. Espy, J.C. Mosher, J.J. Gomez, R.H. Kraus Jr., Microtesla MRI of the human brain combined with MEG, J. Magn. Reson. 194 (2008) 115–120.

[7] B. Blümich, The incredible shrinking scanner, Sci. Am. 299 (Nov) (2008) 92–96.

[8] M. Packard, R. Varian, Free nuclear induction in the earth's magnetic field, Phys. Rev. 93 (1954) 941.

[9] W. Happer, E. Miron, S. Schaefer, D. Schreiber, W.A. van Wijngaarden, X. Zeng, Polarization of the nuclear spins of noble-gas atoms by spin exchange with optically pumped alkali-metal atoms, Phys. Rev. A 29 (1984) 3092–3110.

[10] A.W. Overhauser, Polarization of nuclei in metals, Phys. Rev. 92 (1953) 411–415.

[11] A. Abragam, Principles of Nuclear Magnetism, Oxford University Press, New York, 1989.

[12] C.R. Bowers, D.P. Weitekamp, Transformation of symmetrization order to nuclear-spin magnetization by chemical reaction and nuclear magnetic resonance, Phys. Rev. Lett. 57 (1986) 2645–2648.

[13] J. Clarke, A.I. Braginski (Eds.), The SQUID Handbook, Vol. I: Fundamentals and Technology of SQUIDs and SQUID Systems, Wiley-VCH, Weinheim, 2004.

[14] D. Budker, M. Romalis, Optical magnetometry, Nat. Phys. 3 (2007) 227–234.

[15] D.G. Norris, J.M.S. Hutchinson, Concomitant magnetic field gradients and their effects on imaging at low magnetic field strengths, Magn. Reson. Imaging 8 (1990) 33–37.

[16] M.A. Bernstein, X.J. Zhou, J.A. Polzin, K.F. King, A. Ganin, N.J. Pelc, G.H. Glover, Concomitant gradient terms in phase contrast MR: analysis and correction, Magn. Reson. Med. 39 (1998) 300–308.

[17] D.A. Yablonskiy, A.L. Sukstanskii, J.J.H. Ackerman, Image artifacts in very low magnetic field MRI: the role of concomitant gradients, J. Magn. Reson. 174 (2005) 279–286.

[18] C.A. Meriles, D. Sakellariou, A.H. Trabesinger, V. Demas, A. Pines, Zero- to low-field MRI with averaging of concomitant gradient fields, Proc. Natl. Acad. Sci. USA 102 (2005) 1840–1842.

[19] C.A. Meriles, D. Sakellariou, A.H. Trabesinger, Theory of MRI in the presence of zero to low magnetic fields and tensor imaging field gradients, J. Magn. Reson. 182 (2006) 106–114.

[20] L.-S. Bouchard, Unidirectional magnetic-field gradients and geometric-phase errors during Fourier encoding using orthogonal ac fields, Phys. Rev. B 74 (2006) 054103.

[21] U. Haeberlen, J.S. Waugh, Coherent averaging effects in magnetic resonance, Phys. Rev. 175 (1968) 453–467.

[22] The sample was maintained at −50 °C to avoid dissipating too much power in the heater; there is no inherent difficulty with imaging a room temperature sample with a cryogenic detector [5].

[23] C. Hilbert, J. Clarke, T. Sleator, E.L. Hahn, Nuclear quadrupole resonance detected at 30 MHz with a dc superconducting quantum interference device, Appl. Phys. Lett. 47 (1985) 637–639.

[24] L.-S. Bouchard, M.S. Anwar, Synthesis of matched magnetic fields for controlled spin precession, Phys. Rev. B 76 (2007) 014430.

[25] J. Hennig, A.M. Welz, G. Schultz, J. Korvink, Z. Liu, O. Speck, M. Zaitsev, Parallel imaging in non-bijective, curvilinear magnetic field gradients: a concept study, Magn. Reson. Mater. Phys. 21 (2008) 5–14.

[26] I.M. Savukov, V.S. Zotev, P.L. Volegov, M.A. Espy, A.N. Matlashov, J.J. Gomez, R.H. Kraus Jr., MRI with an atomic magnetometer suitable for practical imaging applications, J. Magn. Reson. 199 (2009) 188–191.

[27] D. Mc Hugh, J. Twamley, Quantum computer using a trapped-ion spin molecule and microwave radiation, Phys. Rev. A 71 (2005) 012315.

[28] C. Wunderlich, G. Morigi, D. Reiss, Simultaneous cooling of axial vibrational modes in a linear ion trap, Phys. Rev. A 72 (2005) 023421.

[29] H. Ciaramicoli, I. Marzoli, P. Tombesi, Quantum spin models with electrons in Penning traps, Phys. Rev. A 78 (2008) 012338.

[30] Slice and volume-selective rotations can be performed in a manner similar to the method proposed in Ref. [20].